ORIGINAL ARTICLE

Impact of initializing the soil with a thermally and hydrologically balanced state on subseasonal predictability

Constantin Ardilouze[1] · Aaron A. Boone[1]

Abstract

Accurate soil moisture initial conditions in dynamical subseasonal forecast systems are known to improve the temperature forecast skill regionally, through more realistic water and energy fluxes at the land-atmosphere interface. Recently, results from a multi-model coordinated experiment have provided evidence of the primal contribution of the initial surface and subsurface soil temperature over the Tibetan Plateau for capturing a hemispheric scale atmospheric teleconnection leading to improved subseasonal forecasts. Yet, both the soil temperature and water content are key components of the soil enthalpy and we hypothesize that properly initializing one of them without modifying the other in a consistent manner can alter the soil thermal equilibrium, thereby potentially reducing the benefit of land initial conditions on subsequent atmospheric forecasts. This study builds on the protocol of the above-mentioned multi-model experiment, by testing three different land initialization strategies in an Earth system model. Results of this pilot study suggest that a better mass and energy balance in land initial conditions of the Tibetan Plateau triggers a wave train which propagates through the northern hemisphere mid-latitudes, resulting in an improved large scale circulation and temperature anomalies over multiple regions of the globe. While this study is based on a single case, it strongly advocates for enhanced attention towards preserving the soil energy equilibrium at initialization to make the most of land as a driver of atmospheric extended-range predictability.

1 Introduction

At the frontier between meteorological and climatic time scales, subseasonal forecasting, often referred to as S2S (Subseasonal to seasonal), remains a challenge for the scientific community. While ocean interannual variability is the dominant source of seasonal predictability at longer lead times, a substantial number of studies have emphasized the key role of continental surfaces in predictability at time scales between two weeks and two months (e.g. Dirmeyer et al. 2015). Soil moisture, in particular, has received special attention since the seminal work of Koster et al. (2004) which identified certain regions of the globe as hotspots of soil moisture-atmosphere coupling. Predictability experiments using numerical models that followed this work such

as GLACE2 multi-model experiment (Koster et al. 2010) and the pilot study from Douville (2010) confirmed that a realistic initialization of soil moisture in dynamic forecasting systems could improve 2-meter temperature forecasts, particularly in so-called "water-limited" semi-arid regions. The snow-atmosphere coupling, which plays a role in the surface radiation and water balance (Xu and Dirmeyer 2013), explains the importance of snow cover initialization for subseasonal forecasting (Orsolini et al. 2013). More recently, a teleconnection has been identified between the surface and subsurface ground temperature of high altitude mountains and precipitation downstream of the flow (Xue et al. 2016, 2018). These findings set the ground for the international initiative 'Impact of Initialized Land Surface Temperature and Snowpack on Subseasonal to Seasonal Prediction Project' (LS4P) (Xue et al. 2021), gathering over 40 partners and more than 20 earth system models around a common experimental forecasting protocol. The phase 1 of LS4P focused on a case study, namely the impact of land surface temperature over the Tibetan Plateau (TP) in May

✉ Constantin Ardilouze
  constantin.ardilouze@meteo.fr

1 CNRM, Université de Toulouse, Météo-France, CNRS, Toulouse, France

2003 on the subsequent drought (flood) occurrence south (north) of the Yangtze river basin in June 2003. The experimental setup consisted in adjusting the TP land temperature at the model initialization step of the subseasonal forecast systems, so as to mitigate the May 2003 surface temperature bias analyzed in a previous baseline control forecast. In this protocol, as well as in other multi-model forecast experiments implying changes in initial soil prognostic variables such as soil moisture (Koster et al. 2011; Ardilouze et al. 2017), the physical consistency between soil prognostic variables at initialization has been overlooked. Inconsistencies may trigger dramatic model-dependent adjustements and partly obscure the outcome of the numerical experiments. Moreover, it prevents disentangling the respective contributions of soil temperature, soil moisture and soil enthalpy (i.e. latent energy) on land-atmosphere coupling and subsequent atmospheric response (Zhao et al. 2018). To tackle this issue, we reproduce the protocol of the LS4P prediction case study with three different initialization strategies detailed in Sect. 2, including their impact on soil variables (Sect. 2.4). Results on atmospheric forecasts are commented in Sect. 3, before a discussion section and concluding remarks.

2 Data and methods

2.1 Subseasonal forecast setup

The four numerical experiments of this study each consist in a 30-member ensemble re-forecast, initialized on May 1st, 2003, and run over a 61-day forecast period, hence until June 30th. They are carried out with the CNRM-CM6-1 earth system model at the standard horizontal resolution which is approximately 150 km (Voldoire et al. 2019). The land component, Interactions between the Soil Biosphere Atmosphere-CNRM Total Runoff Integrating Pathways (ISBA-CTRIP: Decharme et al. 2019), is included in the Externalized Surface (SURFEX: Masson et al. 2013) model and the OASIS-MCT (Ocean Atmosphere Sea Ice Soil—Model Coupling Toolkit) coupler designed to process heat, water and momentum exchanges at the surface (Voldoire et al. 2017). Atmospheric initial conditions are directly derived from the ERA-Interim re-analysis (Dee et al. 2011) while land initial conditions result from an offline 1993-2016 SURFEX simulation forced by 3-hourly ERA-Interim atmospheric fields, as described in Boisserie et al. (2016). Similarly, the $1°$ ocean and sea-ice initial conditions are derived from an ERA-Interim forced ocean run constrained towards the Mercator Ocean International Glorys 2V4 reanalysis (Ferry et al. 2010). The ensemble members are generated through the addition of perturbations to the atmospheric initial conditions. These perturbations are designed

as corrections of model drift errors, following the method described in Batté and Déqué (2016).

2.2 Soil initial state adjustments

In the soil moisture perturbation experiments referred to in the introduction, neither water mass nor enthalpy of the soil are conserved during the initialization process. In this pilot study, an effort is made to use a very simple adjustment methodology to conserve these quantities as best as possible, or to at least have a more physically consistent initial state.

The enthalpy for a soil layer (J m^{-2}) can be defined following (Zhao et al. 2018) as:

$$h = \left[\rho_s c_s \left(1 - w_{sat}\right) + \rho_l c_l w_l + \rho_i c_i w_i\right]\left(T - T_f\right) - \rho_i L_f w_i \quad (1)$$

where T represents the temperature of the soil layer (K), L_f is the specific latent heat of fusion (J kg^{-1}), and w_l, w_i and w_{sat} represent the liquid volumetric water content of the soil, the frozen water and the soil porosity, respectively (m^3 m^{-3}). The densities for liquid water, ice and soil solids are represented by ρ_l, ρ_i and ρ_s, respectively (kg m^{-3}), while c_s, c_w and c_i represent the specific heat capacity of the soil constituents, liquid water, and ice, respectively (J kg^{-1} K^{-1}). The reference temperature corresponds to the freezing point of liquid water, T_f (273.15 K). In Eq. 1, the contribution of air in the soil pores to h has been neglected.

To compute soil water phase changes, ISBA uses the relation between the soil water potential and temperature for sub-freezing conditions from (Fuchs et al. 1978):

$$\psi^* = \psi_{sat} + \frac{L_f \left(T - T_f\right)}{g\,T} \quad (2)$$

where g is the gravitational constant (m s^{-2}), and ψ_{sat} represents the soil matric potential at saturation (m). The potential ψ^* can be substituted in the expression for the soil matric potential in order to obtain the maximum unfrozen (liquid) water content at a given soil temperature. ISBA uses the pedotransfer functions by Clapp and Hornberger (1978) so that

$$w_{l,\max} = w_{sat} \left(\frac{\psi^*}{\psi_{sat}}\right)^{-1/b} \quad (3)$$

where b is related to the slope of the water retention curve. This method is described in more detail in Decharme et al. (2016). Finally, a minimum liquid water content, $w_{l,\min}$ must be defined. Here, it is simply computed as a vegetation-cover weighted average between wilting point (corresponding to a matric potential of -300 m) and a value about half of wilting point. The latter value is an approximation of the minimum value in ISBA generally found in simulations owing to baresoil evaporation.

For LS4P, we first apply a temperature perturbation, ΔT, to soil layers in a masked region. Then the soil water and ice contents are adjusted to either conserve enthalpy which corresponds to the newly imposed temperature or the soil moisture components are adjusted in order to result in a state which is closer to a thermal equilibrium (or at least what is deemed to be more physically realistic in terms of wetting-cooling or drying-warming). The four possible responses of h to the application of a ΔT using the methodology herein can be summarized as follows:

- 1 A potentially frozen soil thaws owing to the application of a sufficiently large ΔT. Any soil ice is simply removed thus a warming soil is becoming potentially more dry. Mass is not conserved if the original state had soil ice. Note that using the definition of enthalpy in Eq. 1, h conservation is not possible in this pathway as it changes sign.
- 2 A soil with a temperature initially above T_f cools to below freezing. As in case 1, h conservation is not possible, but mass is potentially conserved: the partitioning between frozen and unfrozen soil water is made by imposing $w_l \leq w_{l,max}$ where the maximum liquid water content for $T > T_f$ is defined using Eq. 3.
- 3 Both the initial and final soil temperatures are above freezing. There is no soil ice initially so that warming/cooling correspond to drying/wetting by simple inversion of Eq. 1 for w_l using the new T. Mass is not conserved, but enthalpy is unless the final adjusted w_l value either exceeds saturation, w_{sat}, or falls below some minimum value, $w_{l,min}$ (described in more detail below).
- 4 Both the initial and final soil temperatures are below freezing. In a first step, the total mass is conserved but the partitioning between ice and liquid soil water is modified to conserve enthalpy. The ice content is first diagnosed under this assumption by solving Eq. 1 for w_i. The soil ice is then checked to see if it exceeds physical limits (totally frozen soil or negative soil ice). In this case, the ice is limited and liquid water is adjusted to conserve enthalpy (and mass). As in case 3, if after adjustment the liquid water exceeds physical limits, it is limited thus both mass and enthalpy conservation imbalances can occur.

These pathways are represented by arrows in the left-hand panel of the schematic shown in Fig. 1. Indeed, when the imposed temperature change ΔT leads to the crossing of the freezing temperature threshold T_f (meaning going from sub-freezing temperatures to freezing or vice versa), the soil enthalpy can no longer be conserved using the definition of enthalpy in Eq. 1 (i.e. using a reference temperature of T_f) together with the fact that we are attempting to preserve the temperature anomalies. Note that in reality, latent heat
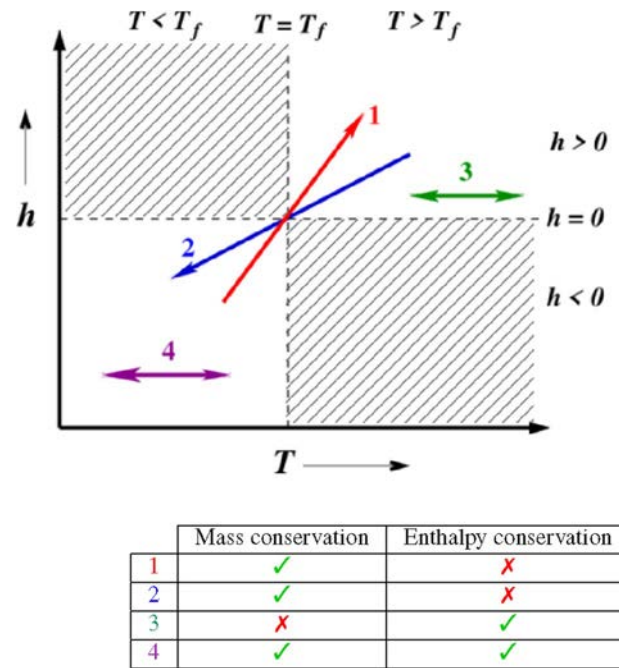

Fig. 1 Schematic of the four possible scenarios for soil enthalpy, h, change when initial soil temperature T is modified through the application of a temperature change in LS4P$_{phy}$. T_f represents the freezing point temperature. The dashed quadrants are deemed to be physically impossible. The physically-based limits prevent enthalpy conservation in cases 1 and 2: liquid water mass is conserved for case 1 (ice is removed if initially present), and total mass is conserved for Case 2 unless physical limits of the final adjusted moisture state are exceeded. Cases 3 and 4 allow enthalpy conservation with adjustments (to soil water content) if physical limits are exceeded. If adjustments are indeed required (for example, to avoid super saturation or over-drying resulting from the first pass at enthalpy conservation), enthalpy might not be conserved

changes (going between frozen and unfrozen soil states) would balance input heating or cooling. The Table in Fig. 1 summarizes the four possible pathways for the LS4P$_{phy}$ experiment and which quantities are conserved (or not).

2.3 Sensitivity experiments and reference data

The baseline (Ctrl) experiment corresponds to the setup described in Sect. 2.1, and the 3 additional experiments only differ from the Ctrl case through changes in land initial conditions over the TP. In LS4P$_t$, a temperature correction mask (Fig. 2c) is applied to the 14 soil layers of ISBA-CTRIP, corresponding to the default 10-m soil depth. The underlying idea of this correction is to reduce the average cold bias of the model affecting the TP. This positive temperature mask was generated following the method described in the section 3.2.3 of Xue et al. (2021). It was calculated by taking into account both the average cold bias over the entire TP (Fig. 2b) and the cold observed anomaly (Fig. 2a). The LS4P$_{phy}$ experiment consists in adjusting soil liquid water

Fig. 2 a May 2003 observed monthly mean 2-m temperature anomaly, **b** difference between the Ctrl ensemble mean and the observation, **c** and soil temperature correction mask applied at initialisation. Unit: K
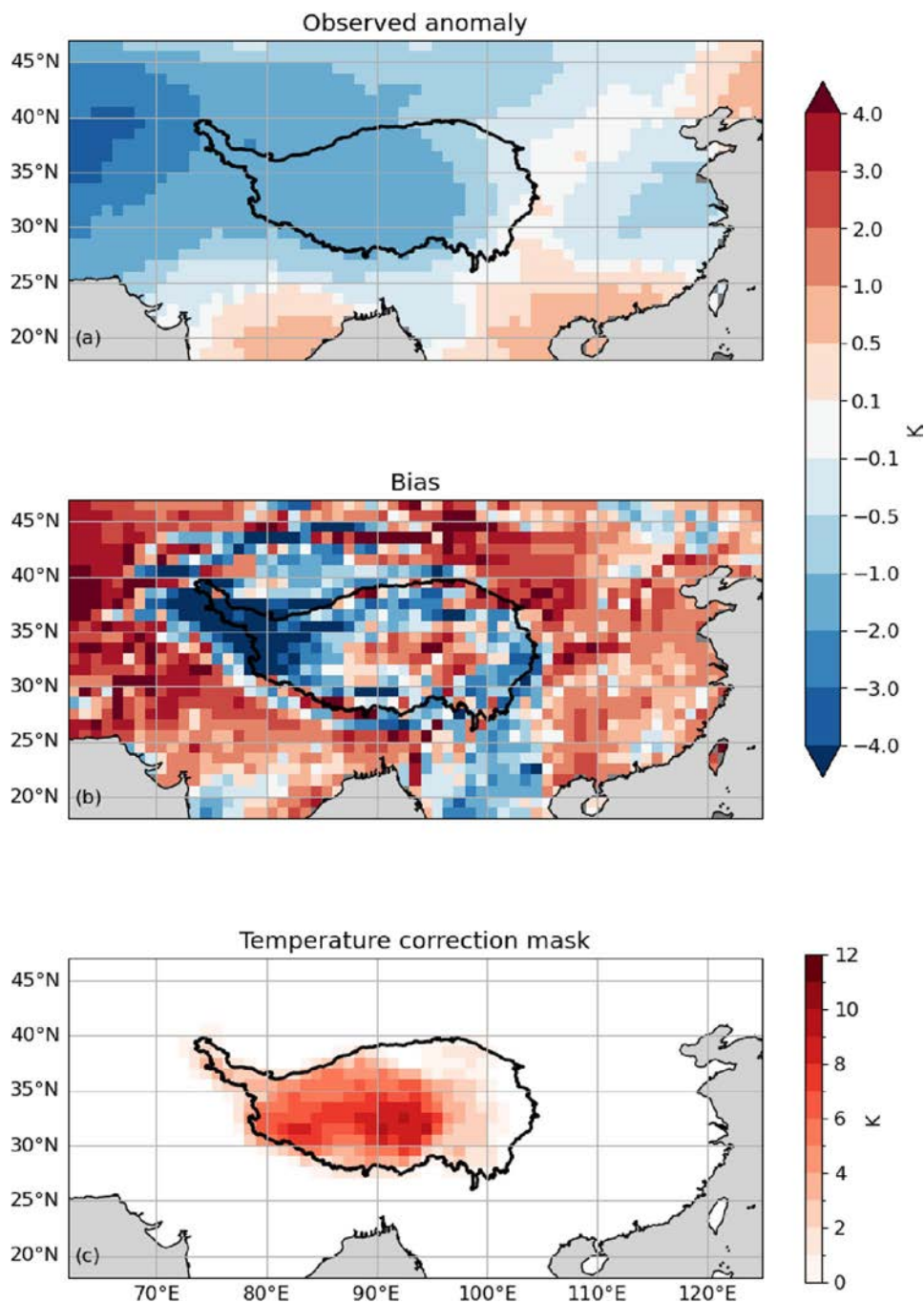
and ice content while applying the prescribed temperature correction, in order to impose physical consistency and/or enthalpy conservation, to the maximum possible extent.

Finally, the last sensitivity experiment, LS4P$_{sm}$, consists in adjusting the soil moisture over the TP as in LS4P$_{phy}$, but without applying the soil temperature correction. For example, soil is dried (wetted) if a positive (negative) temperature change was prescribed by LS4P. Thus, this experiment is somewhat akin to a GLACE type experiment in that only the soil water content is modified, but in a manner

consistent with the temperature corrections (thus differing from GLACE in this respect). The aim of LS4P$_{sm}$ is to provide insight on the respective contributions of the initial soil temperature and soil moisture over the TP in subseasonal forecasts. Table 1 recapitulates, for each experiment, the soil prognostic variables that are changed at initialization.

In this study, three reference datasets are used to evaluate our simulations. The 2-meter temperature (t2m) is assessed against version 4 of the monthly gridded CRU-TS dataset (Harris et al. 2020) and precipitation is evaluated using the

Table 1 List of experiments and prognostic variables which are potentially adjusted at initialization over the TP

	Soil temperature	Soil liquid water	Soil ice
Ctrl	×	×	×
LS4P$_t$	✓	×	×
LS4P$_{sm}$	×	✓	✓
LS4P$_{phy}$	✓	✓	✓

monthly multi-source MSWEP V2 (Beck et al. 2019) dataset. The ERA5 reanalysis (Hersbach et al. 2020) is used as the reference for atmospheric fields on standard pressure levels. Simulation output and reference data have been re-gridded onto a common 1x1° regular rectangular grid.

The comparison of 2003 subseasonal re-forecasts with observational counterparts is based on anomalies relative to the 1993–2016 period rather than the 2003 full fields, which is a standard bias correction strategy. In that respect, the model climatology is computed from an extension of the Ctrl re-forecast to all the other years of the 1993–2016 period,

with the same initialization day (May 1st), and following the setup described in Sect. 2.1.

2.4 Impact on land prognostic variables

To verify the validity of our setup, we first analyze the vertical profile of land prognostic variables after one day of model integration. In Fig. 3, only the profile for the top first meter of soil is displayed since it has an impact on land-atmosphere interactions over the S2S timescale. Although initial soil temperature is unchanged in LS4P$_{sm}$ (green line) with respect to the Ctrl (black), the temperature profile appears slightly shifted towards higher values (Fig. 3c) due to the latent heat release owing to soil water freezing occurring during the first steps of the model integration. This is supported by the slightly higher ice content and lower liquid water content profiles (Figs. 3b and 3a, respectively) in LS4P$_{sm}$, as compared to LS4P$_{phy}$ (orange line), despite their identical change in initial soil water content. The difference in the temperature profile between LS4P$_t$ (blue line) and LS4P$_{phy}$ (orange line) is also significant, considering their
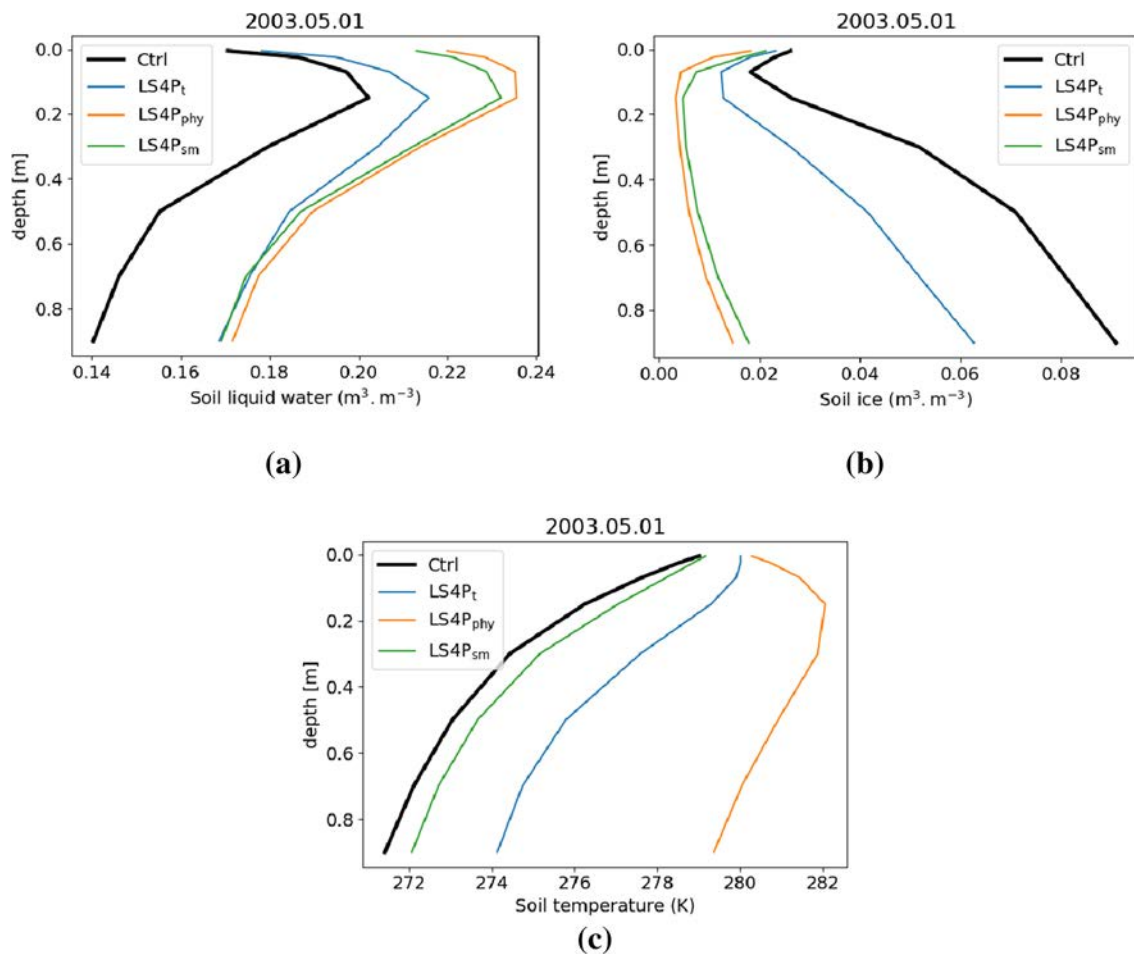

Fig. 3 Liquid water (**a**), ice (**b**) and temperature (**c**) soil profile averaged over the TP on May 1st 2003

similar initial temperature corrections. This pronounced drop in temperature relates to soil ice thawing in LS4P$_t$, which explains the difference with Ctrl in soil ice profile (Fig. 3b) and liquid water profile (Fig. 3a). Thus, there is a large physical adjustment owing to an initial state which is not in thermal equilibrium. Note that the four temperature profiles are relatively close to each other near the surface, because of the rapid adjustment to the overlying atmospheric conditions after the first day of model integration.

Not surprisingly, the evolution of the land prognostic state variables throughout the 2-month forecast time (Fig. 4) shows a progressive decrease of the soil ice content in the uppermost m of the soil for the Ctrl and LS4P$_t$, in agreement with the seasonal atmospheric warming occurring from late spring to early summer (Fig. 4b). In response to ice thawing, soil liquid water in LS4P$_t$ and Ctrl progressively increases with time (Fig. 4a). While the soil moisture content remains nearly identical for LS4P$_{sm}$ and LS4P$_{phy}$, the latter is substantially warmer at all times, despite a decreasing trend during the first 15 days (Fig. 4c). LS4P$_{sm}$ starts as cool as

in Ctrl, by construction, but ends up slightly warmer than LS4P$_t$. This relates to the abundant soil ice in the early stage of LS4P$_t$ which cools down the land surface mainly due to ice thawing in May, and evaporation of a relatively moist soil in June. The mean snow cover over the TP (Fig. 4d) evolves consistently, i.e. the warmer the soil, the lower the snow water equivalent. Due to relatively cold soil conditions in LS4P$_{sm}$ during the first half of the period, the average snow pack remains close to Ctrl and starts diverging afterwards. However, although the soil becomes progressively warmer than LS4P$_t$, the seasonal decline of the snow cover does not catch up, because the amount of accumulated snow at the beginning of the melting season (~ May 20th) is higher than in the other sensitivity experiments. Note that in the current study, the soil states are modified while holding the snow properties (mass, snow pack enthalpy, liquid content...) constant between the original and perturbed setups. But owing to the feedbacks between the soil and snow pack, we plan to investigate perturbing the snow pack properties along with the soil in the next phase of LS4P.
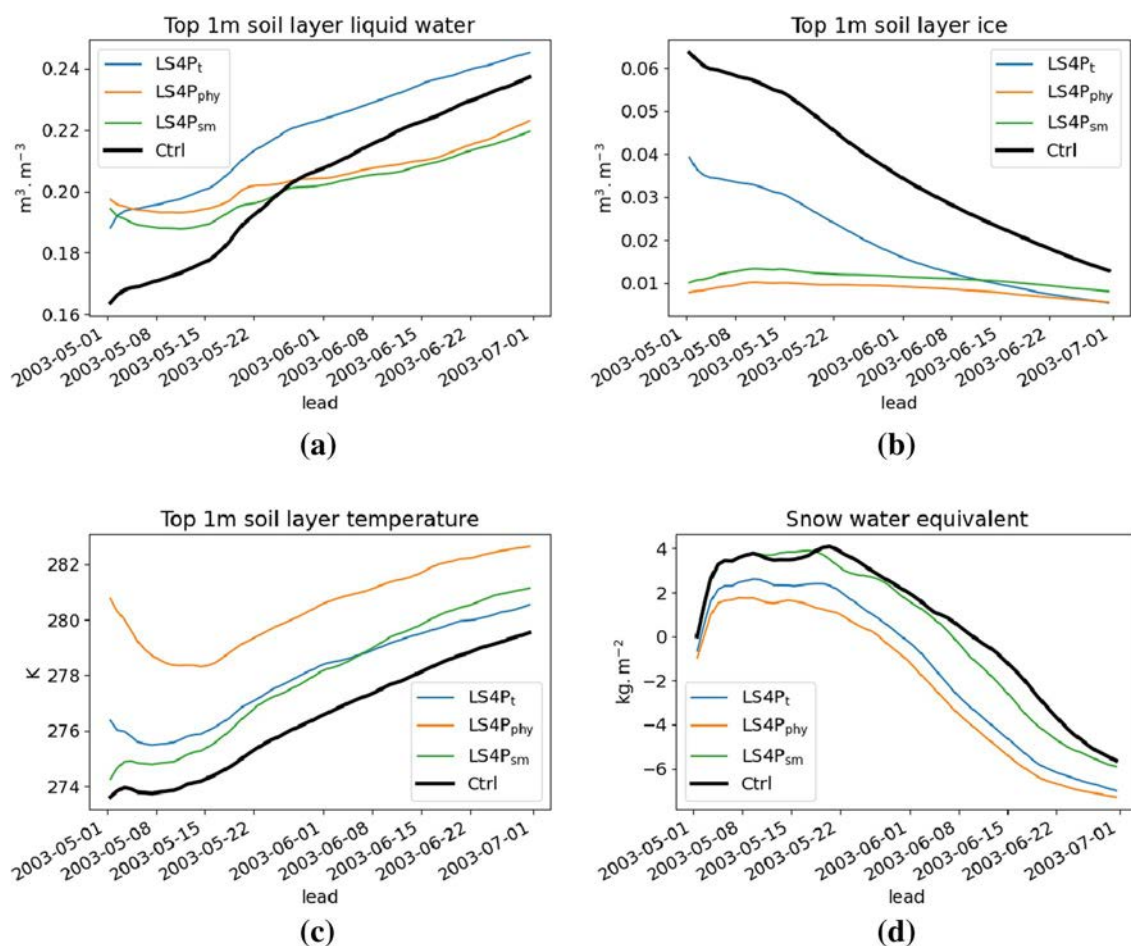

Fig. 4 Ensemble mean evolution of top 1 m liquid water (**a**), ice (**b**), temperature (**c**) and snow water equivalent departure from the initial Ctrl value (**d**) over the TP

3 Results

In this section, we analyze the atmospheric response to the land initialization strategy over the TP. For each simulation, the ensemble mean is considered. The statistical significance of the difference between two simulations is assessed by means of a two-sided Student's t-test for paired samples. Here, the samples correspond to the 30 ensemble members of the simulations. The null hypothesis is rejected for p-values exceeding 0.05. The comparison of the simulations with observational references is based on pattern anomaly correlation calculated over the entire northern hemisphere and 3 sub-regions: North America (140°W-60°W,25°N-60°N), Europe (15°W-45°E,30°N-70°N) and East Asia (80°E-140°E,20°N-55°N). The boundaries of these regions are depicted in Fig. 5a-1. The observed anomalies are relative to the observed climatology over the 1993–2016 period, while the simulated anomalies are relative to a model climatology, derived from a full hindcast initialized on May 1st for each year of the 1993-2016 period, following the setup described in Sect. 2.1. This manner of comparing anomalies rather than full fields is a standard bias-correction procedure in the evaluation of subseasonal forecasts (e.g. Domeisen et al. 2022). Note that for assessing the statistical significance of pattern correlations, we take into account the spatial autocorrelation between adjoining grid points (Wilks 2011). As a consequence, the effective sample size of grid points retained to compute the the t-statistic is higher for spatially heterogeneous fields (precipitation), than for smoother fields (temperature or geopotential height). Thus, for similar correlation values, the precipitation pattern correlation is more likely to be significant than the geopotential height at 500 hPa (z500) or temperature counterparts (see Table 2).

3.1 Evaluation of the Ctrl forecast for May and June 2003

The Ctrl re-forecast simulation is compared to observations for t2m, precipitation and mid-troposphere circulation patterns (Fig. 5). As expected, the magnitude of the June 2003 Ctrl anomaly patterns (sub-figures a-4, b-4 and c-4) are weaker than the May counterpart (a-3, b-3 and c-3): indeed, due to the chaotic nature of the atmosphere, the forecast members tend to diverge with time and therefore the ensemble spread is larger in June than in May. The warm anomaly observed in May and June over Europe corresponds to the early stage of the extremely hot summer of 2003 (Black et al. 2004). The anomaly pattern correlations reported in Table 2 confirm that Ctrl compares remarkably

well with observations in May, while to a lesser extent in June, where a spurious cool anomaly is forecast over the Iberian peninsula. The wet-North dry-South pattern, as well as the southern Europe anticyclonic blocking, are also well captured by the model in May, resulting in very high correlations for precipitation and z500. In June, a weaker, but significant signal is still found over central Europe for precipitation. More generally, the correlations drop substantially in June for most of the considered variables and regions, which is not surprising, given that the May correlations are augmented by the higher predictability of the first 10 days after initialization belonging to the meteorological predictability horizon. Over the rest of the northern hemisphere, the temperature patterns are less well captured by Ctrl with a few local exceptions like over north-west America, Asian steppes and western Africa in May. The shift from dry May to wet June anomalies north of the Gulf of Guinea is very well simulated by Ctrl. Finally, the z500 patterns are very well captured over Europe and East Asia in May but less so over North America, and conversely in June, when Ctrl succeeds in simulating the positive anomaly near the West coast of North America (Fig. 5c-4).

3.2 Impact of the TP land initialization strategy

In May 2003 (Fig. 6a), the three perturbed simulations show a significant impact on t2m over North America. While they all tend to amplify the Ctrl warm bias from the Hudson Bay to New England, only LS4P$_{sm}$ and LS4P$_{phy}$ mitigate the cold bias over the western US. Additionally, LS4P$_{phy}$ simulates a cooler pattern over much of the south-east US affected by a pronounced warm bias in Ctrl. This is confirmed by the increased pattern correlation in Fig. 7a. Elsewhere, none of the simulations particularly outperforms the other ones except for LS4P$_t$ which improves temperature patterns over East Europe and West Russia. At the northern hemisphere scale, all the simulations are fairly even in terms of statistically-based performance. In June 2003 (Fig. 6b), the signal is weaker over America, and the simulations do not reduce the strong warm bias over Central US, a classic summer pattern in many climate models (e.g. Zhang et al. 2018). The bias is even accentuated in LS4P$_t$ and LS4P$_{phy}$ to a lesser extent. Over Eurasia, the three simulations show warmer t2m north east of the Caspian Sea but only LS4P$_{phy}$ partly compensates the cool bias over the Iberian peninsula and Central Siberia. This simulation also performs better over the TP, North China and Lapland. The t2m pattern correlation (Fig. 7b) further underscores the good performance of LS4P$_{phy}$ over these regions in June.

A similar analysis for precipitation also indicates a strong impact of our experimental setup in May 2003 over North America (Fig. 8a), with LS4P$_{sm}$ and LS4P$_{phy}$ showing

Fig. 5 Comparison of May and June 2003 observed and Ctrl anomalies for (**a**) 2-meter temperature in K, (**b**) precipitation in mm/day and (**c**) 500 hPa geopotential height (m)
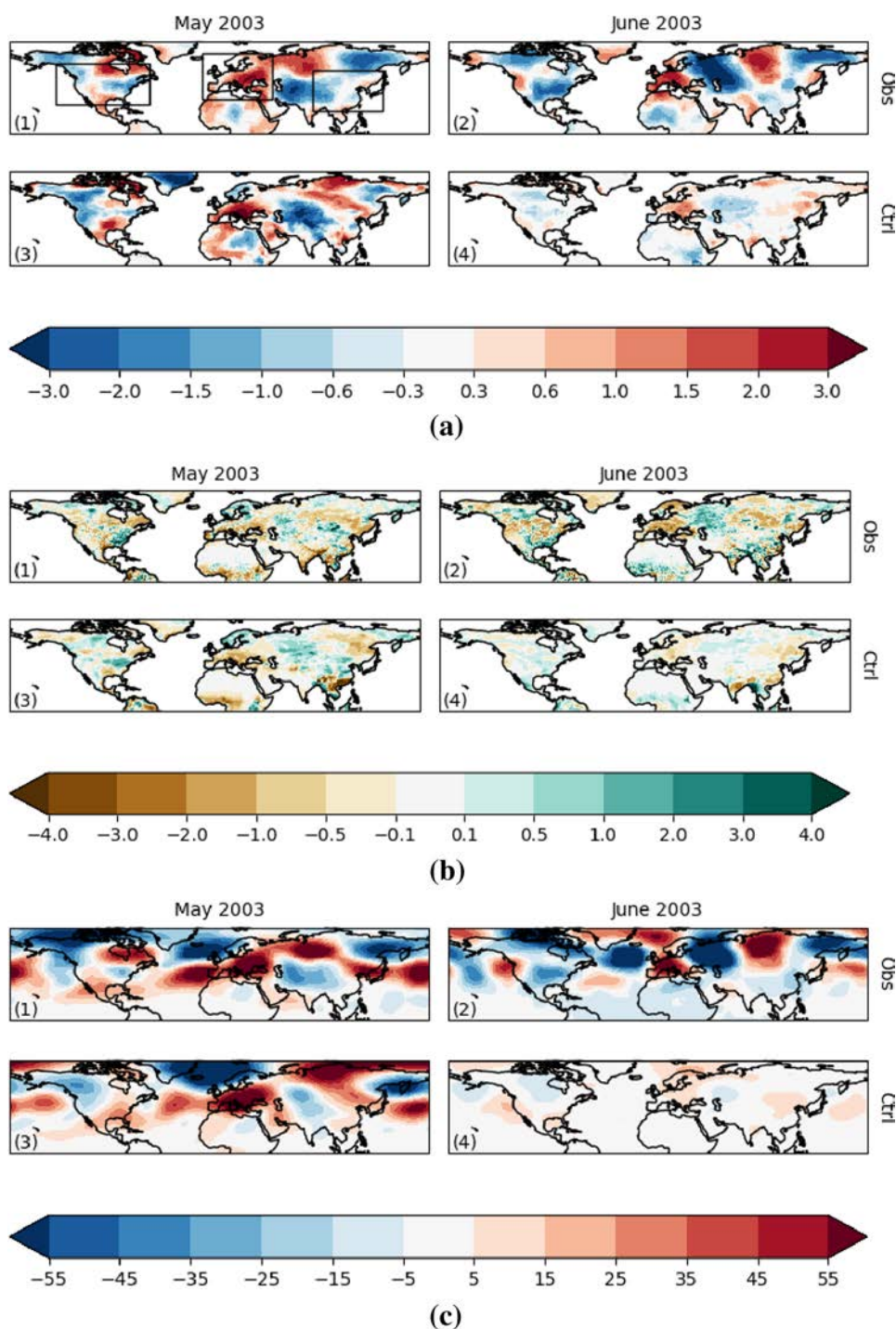
enhanced mitigation of the wet bias over the Rockies and Great Plains. In June 2003, the signal is weak overall (Fig. 8b). However, LS4P$_{phy}$ indicates several local improvements. More precisely, this simulation captures a dryer pattern over central Siberia, and a wetter pattern over northern India, western Sahel and north of the Yangtze, keeping in mind that the latter regions are affected by a strong dry bias in Ctrl. The markedly wet bias over Myanmar is mitigated in both LSP$_t$ and LS4P$_{phy}$. For all of the large-scale focus regions, the pattern correlations do not reveal any substantial difference between simulations (not shown). However, the aforementioned regional improvements in LS4P$_{phy}$ suggest a rather beneficial impact of this land initialization strategy also for the precipitation forecast. The local improvements captured nearby the Yangtze river are further commented at the end of Sect. 3.3.

Table 2 Spatial anomaly correlation of Ctrl with Obs in May (M) and June (J) 2003. The bold font highlights positive Values which are significant at the 95% confidence level

	2-m temperature	Precipitation	z500
Northern hemisphere	M:**0.44** J:**0.31**	M:**0.23** J:0.17	M:**0.49** J:0.23
North America	M:0.42 J:−0.04	M:**0.28** J:**0.14**	M:**0.29** J:**0.46**
Europe	M:**0.59** J:0.28	M:**0.62** J:**0.23**	M:**0.89** J:−0.1
East Asia	M:**0.50** J:0.08	M:**0.14** J:**0.16**	M:**0.81** J:0.03

The t2m and precipitation patterns described above are partly driven by changes in the atmospheric circulation The maps for z500 (Fig. 9) reveal differences with a larger amplitude in May, especially over the western north hemisphere.

Differences are weaker for LS4P$_t$, though. The LS4P$_{phy}$ map suggests a wave-like pattern. This feature will be commented in the following section. For this simulation, the regional correlations indicate substantially improved circulation anomalies across North America (Fig. 10a), but no particular impact elsewhere.

In June (Fig. 9b), the sensitivity experiments exhibit overall less widespread differences with respect to Ctrl. However, here again, LS4P$_{phy}$ distinguishes itself from the other simulations owing to a relatively marked geopotential anomaly tripole composed by a central positive anomaly stretching across southern Siberia and two negative anomalies over Northern Europe and, more weakly, from northern China to north-west Pacific. This feature is also visible in LS4P$_{sm}$ and LS4P$_t$, but with barely, if

Fig. 6 **a** May 2003 and **b** June 2003 t2m differences (top row) LS4P$_t$ minus Ctrl, (middle row) LS4P$_{phy}$ minus Ctrl and (bottom row) LS4P$_{sm}$ minus Ctrl, in K. Hatching indicates statistically significant values at a 95% confidence level from a 2-sided t-test
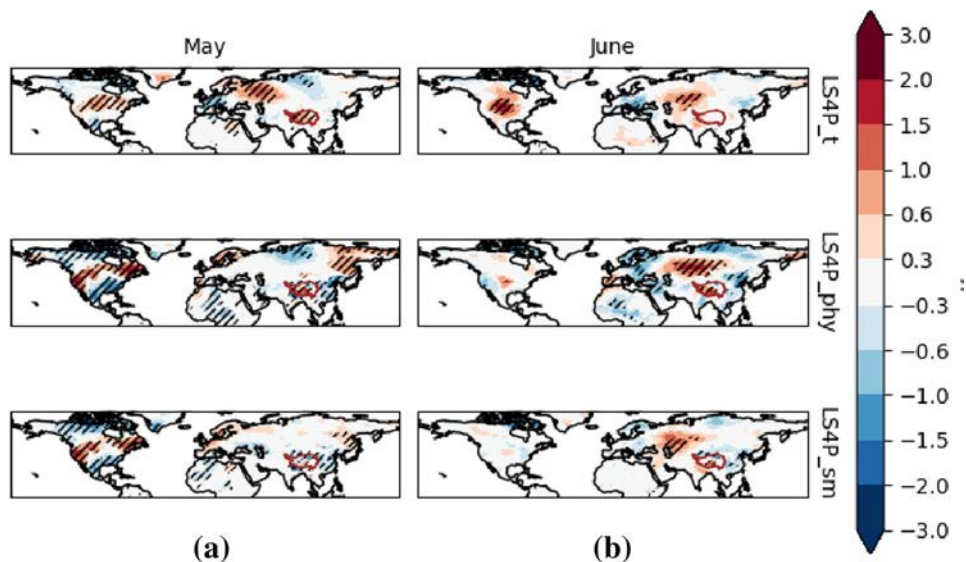

Fig. 7 **a** May 2003 and **b** June 2003 t2m anomaly pattern correlation with ERA5, by domain. Bold values are statistically significant at a 95% confidence level
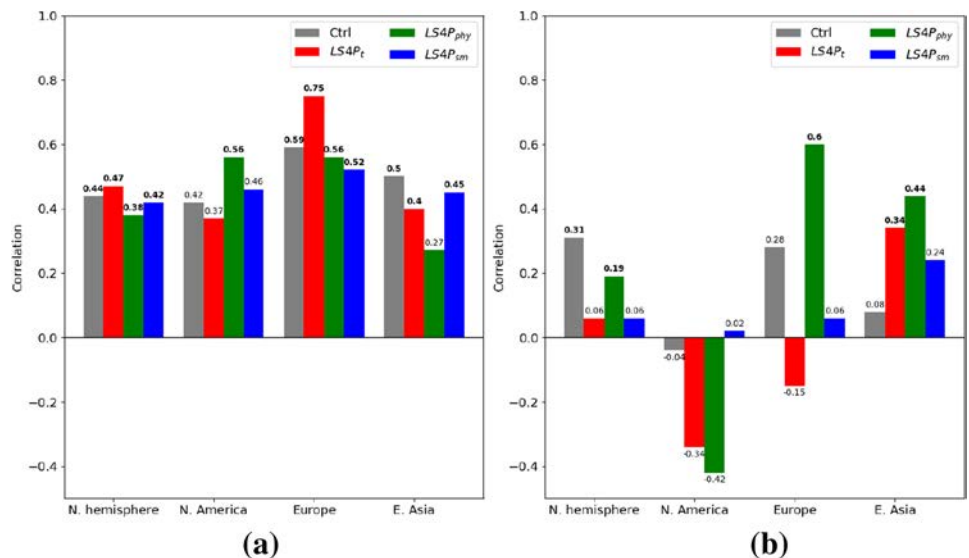
Fig. 8 As figure 6 for precipitation (unit: mm/day)
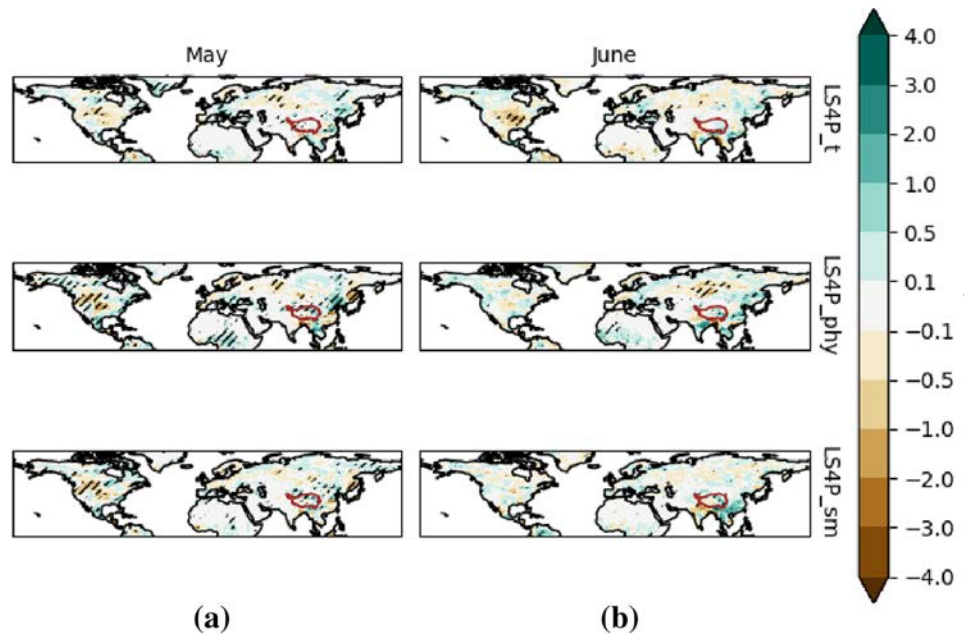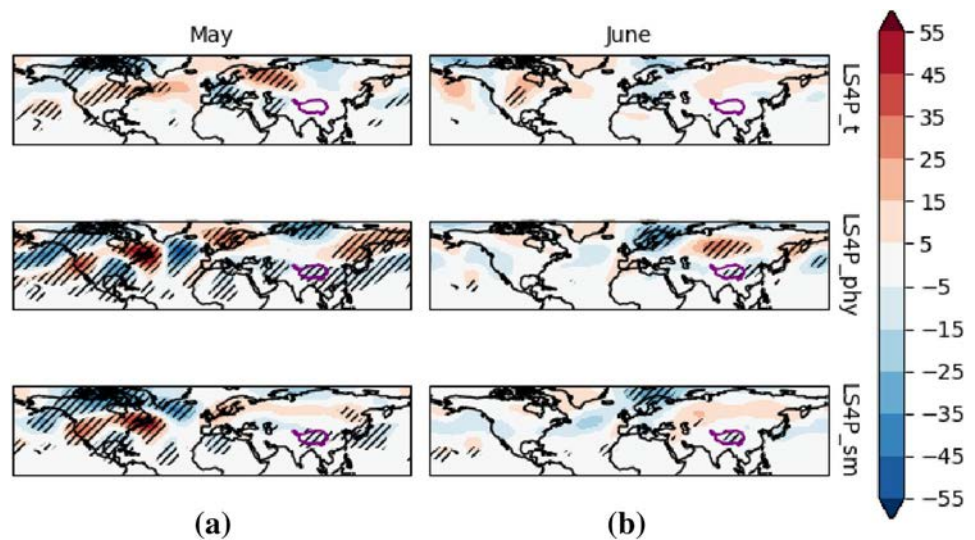

**Fig. 9** As figure 6 for geopotential height at 500 hPa (unit: m)

at all, any significant patterns. The pattern correlations reveal that LS4P$_{phy}$ considerably improves the circulation anomaly over both Europe, thanks to lower geopotential height over Scandinavia, and East Asia. This result is consistent with the t2m analysis.

The relatively higher performance of the Ctrl simulation over North America in June is largely due to the successful simulation of the z500 positive anomaly located near the west coast of America. A possible reason for the poorer results of the sensitivity experiments in this respect is discussed in Sect. 4.

3.3 Description of the mechanisms involved

In the previous section, we identified a number of common features between the sensitivity experiments: the adjustement of land initial conditions over the TP affects mainly the western half of the northern hemisphere during the first month of the forecast, and the eastern half during the second month, albeit less markedly. The adjustment strategy impacts mainly the amplitude and location of atmospheric anomaly patterns, which translates into reduced or increased biases.

Fig. 10 **a** May 2003 and **b** June 2003 z500 anomaly pattern correlation with ERA5, by domain. Bold values are statistically significant at a 95% confidence level

(a)

(b)
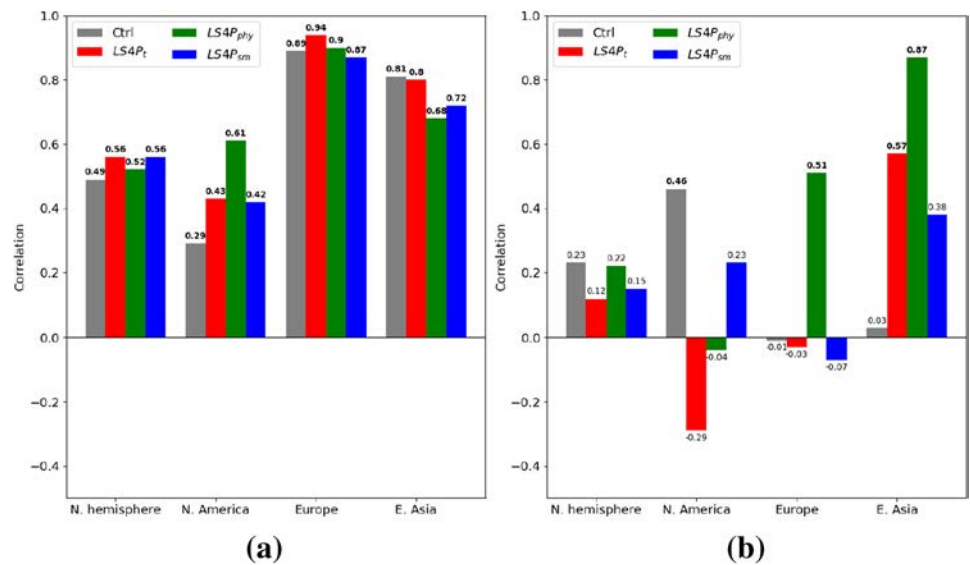
As suggested earlier, a striking feature of the change in z500 circulation over North America in May 2003 for LS4P$_{phy}$ is a wave-like pattern. Additionally, it is remarkably out-of-phase from the Ctrl bias pattern (the pattern correlation value between the z500 bias and the LS4P$_{phy}$ z500 anomaly over the North America domain is −0.74). This is also true for LS4P$_{sm}$ but to a lesser extent, especially for south-East US (spatial correlation value: −0.48). The anomaly pattern found in LS4P$_{phy}$ matches very well with the Tibetan Plateau-Rocky Mountains Circumglobal (TRC) wave train identified by Xue et al. (2022) (Their Fig. 4B) and named as such in (Xue et al. 2023,thisissue). In June (Fig. 9b), the relative agreement between sensitivity simulations on a geopotential anomaly tripole described earlier and

stretching from Northern Europe to Northern China suggests that the TRC, identified as a May teleconnection pattern, can propagate in June across Eurasia. In the upper troposphere, the geopotential height anomaly is affected consistently by the mid-troposphere (Fig. 11), and consequently, the jet stream is shifted northwards in May over North America and in June over Asia, with a stronger amplitude in LS4P$_{phy}$.

In order to illustrate the dynamic propagation, we show the time evolution of 250 hPa meridional wind anomalies from Ctrl, averaged out over the 30°N-60°N meridional cross-section (Fig. 12). The three perturbed simulations clearly show a wave train emerging from the TP longitudes and propagating eastwards during the first 30 days. This wave train is very weak in LS4P$_t$ and rapidly fades out while
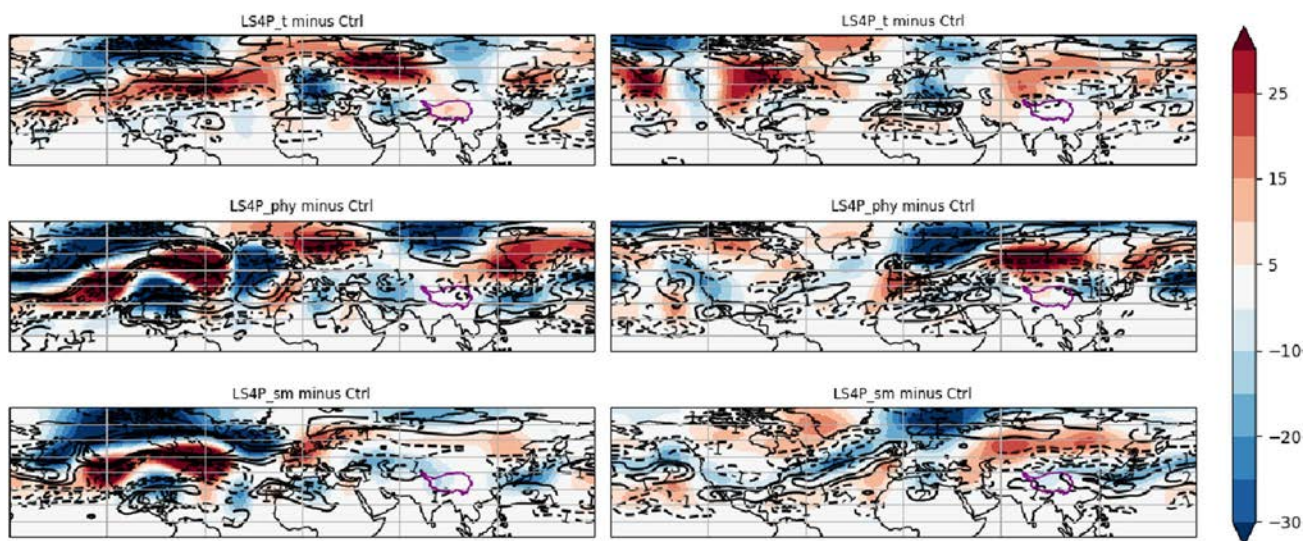

Fig. 11 May (left column) and June (right column) 2003 250 hPa geopotential height (shade) and zonal wind (contour) anomaly
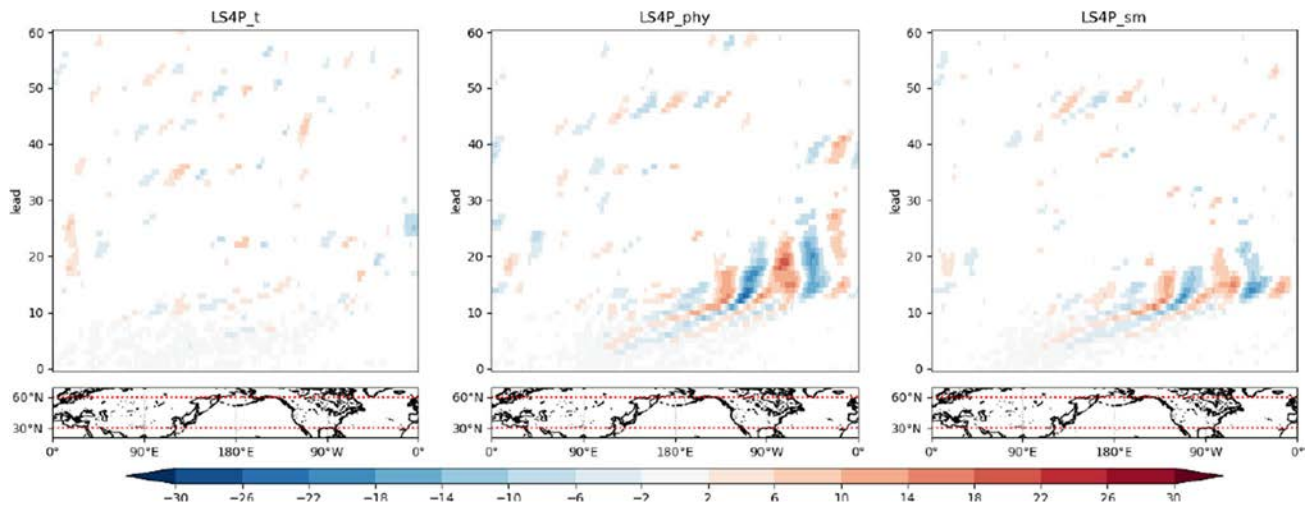
Fig. 12 Hovmöller diagrams of 250 hPa meridional wind anomaly averaged between 30°N and 60°N. Values not significant at the 95% have been set to 0

on the other hand, it is particularly strong in LS4P_phy. The attenuated wave train re-emerges past day 40 in longitudes stretching eastwards from Central Asia to the North Pacific. Again, it is the strongest and best established in LSP_phy. The choice of a cross section bounded between 30°N and 60°N was a trade-off to include most of the TP and mid-latitudes, without averaging out too many opposite anomalies, that could mask the signal. The drawback is that the wave propagation at higher latitude across northern Scandinavia and Lapland, if any, is not detectable. This could explain the discontinuity found in wave propagation illustrated in the Hovmöller diagram between day 25 and day 40 after initialization. A similar Hovmöller analysis has thus been achieved for a cross section between 55°N and 75°N (Fig. 13). It reveals an eastward wave propagation between day 25 and

day 45 after initialization from the Greenwich meridian to 80°E. This wave propagation is more pronounced in LS4P_phy than in other perturbed experiments.

The way land surface is initialized over the TP in early May is therefore susceptible to trigger an extratropical circumglobal atmospheric wave train. This wave train considerably modifies the atmospheric flow in our model for several weeks.

Finally, even if the impact of our experiments on continental south East Asia precipitation remains inconclusive, the potential interaction with the onset and evolution of the East-Asian monsoon cannot be discarded, and in particular one of its main components known as the Meiyu-Baiu front. This quasi-stationary area of intense rainfall forms in spring at the confluence of the summer monsoon moist air south of
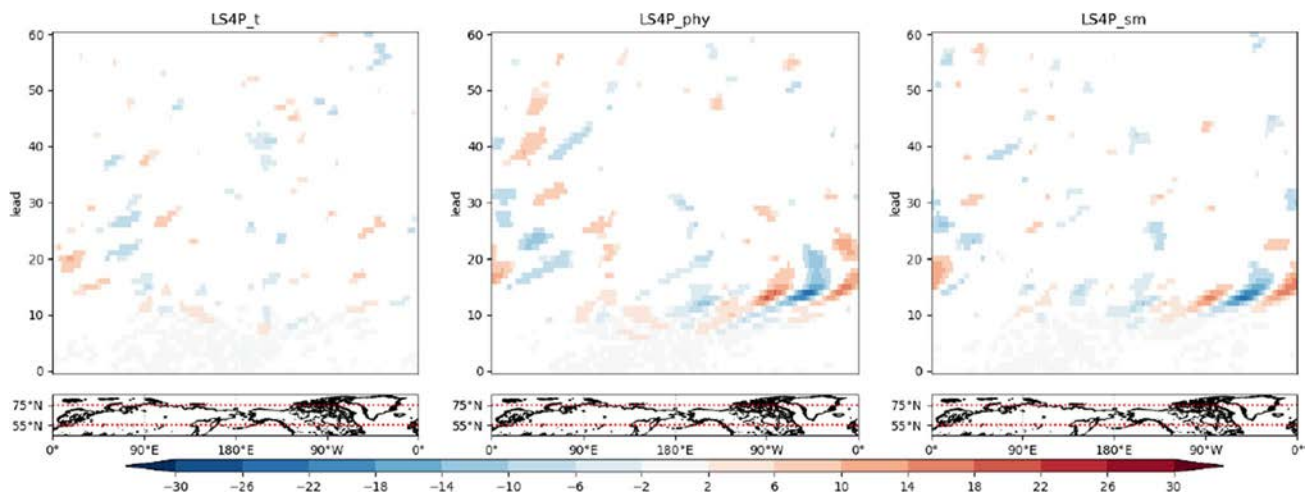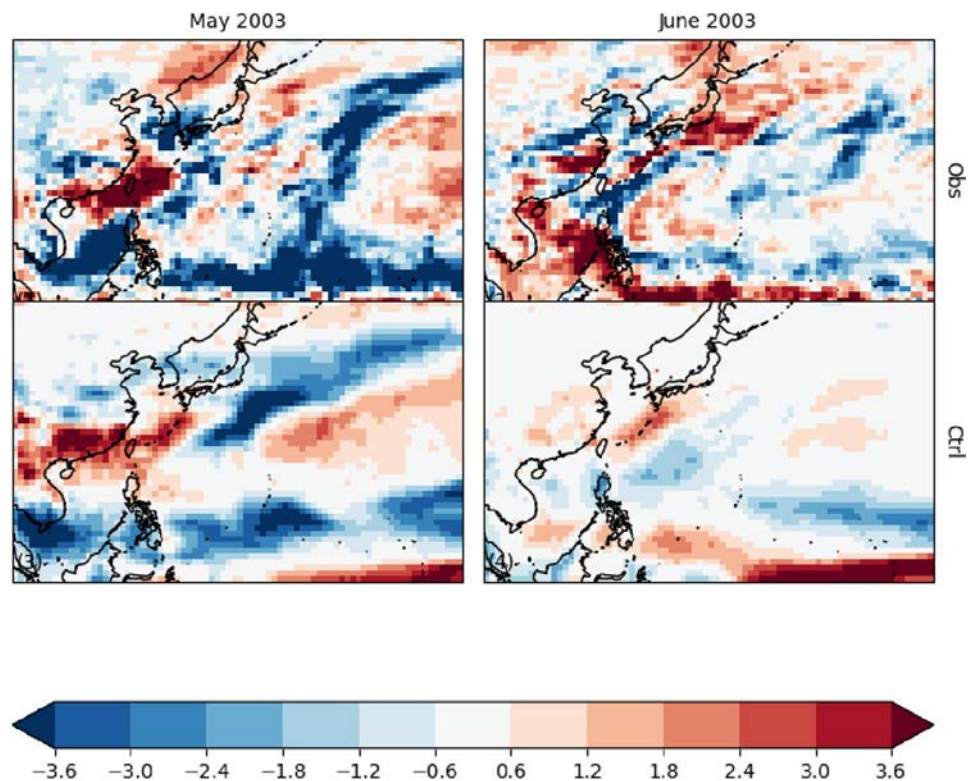

Fig. 13 As figure 12 between 55°N and 75°N

China and the warm dryer air to the North (e.g. Zhou et al. 2004). The location and evolution of the Meiyu-Baiu front is governed by a wide range of factors covering multiple scales, including the thermal forcing of the TP (e.g. Liu et al. 2007), as well as the mid-latitude westerly jet (Sampe and Xie 2010). In this study, both factors are impacted by the TP land initialization, and could thus change the location and intensity of this front. In Fig. 14, we show the anomaly of vertically integrated moisture divergence in ERA5 and Ctrl, in order to localize the Meiyu-Baiu front. In May, Ctrl captures relatively well the divergence (convergence) anomalies in red (blue) shades, corresponding to dry (wet) spells, especially over the China sea. The strip of moisture convergence simulated south of Japan is mislocated and too zonally tilted with respect to observations. The location is partly improved in LS4P$_{phy}$ and LS4P$_{sm}$ with a south-eastward shift of this convergence front (Fig. 15a). This shift results from the change in large-scale circulation, and in particular the meridional displacement of the subtropical westerly jet (Sampe and Xie 2010). More precisely, in these two simulations, the wave propagation triggers the development of a barotropic low pressure anomaly between China and Southern Japan at 500 hPa (Fig. 9a), and to a lesser extent at 250 hPa, in the lee of the TP (two bottom-left maps of Fig. 11). Accordingly, the subtropical westerly jet is accelerated south of this low anomaly, which favors the southwards advection of cool dry air from the mid-latitudes. Eventually, the convergence with northward monsoonal flow is shifted further south than in

the Ctrl experiment. This result is consistent with the study from Volonté et al. (2022) highlighting the sensitivity of the Meiyu-Baiu front location to the transient mid-latitude weather disturbances steered by the westerly jet.

In June (Fig. 15b), the observed moisture divergence anomaly is rather patchy, suggesting a little organised Meiyu-Baiu front. Over China, the dry (wet) anomalies located south (north) of the Yangtze river materialize the exceptional drought (precipitation) that motivated the choice of the year 2003 as the initial case study of LS4P (Xue et al. 2021). Ctrl misses these anomalies and simulates a convergence anomaly north-east of the Philippines, where observations indicate a anomalously dry pattern (red shades). This is partly improved in LS4P$_t$ and LS4P$_{phy}$ where dryer conditions are simulated. It is noteworthy that LS4P$_{phy}$ simulates a strip of enhanced moisture convergence north of the Yangtze and conversely further south. This could be related to the improved z500 circulation pointed out in Sect. 3.2, but considering the small scale of these features, verification of any relationship would require further analysis beyond the scope of the current study.

4 Discussion and conclusion

We have revisited the LS4P exercise (Xue et al. 2021) which consists in adjusting the land initialization over the Tibetan Plateau (TP) in ESM-based late spring subseasonal

Fig. 15 a May and **b** June 2003 vertically integrated moisture divergence (shade) in kg.m^{-2}.day^{-1} and 850 hPa wind anomalies (vectors)
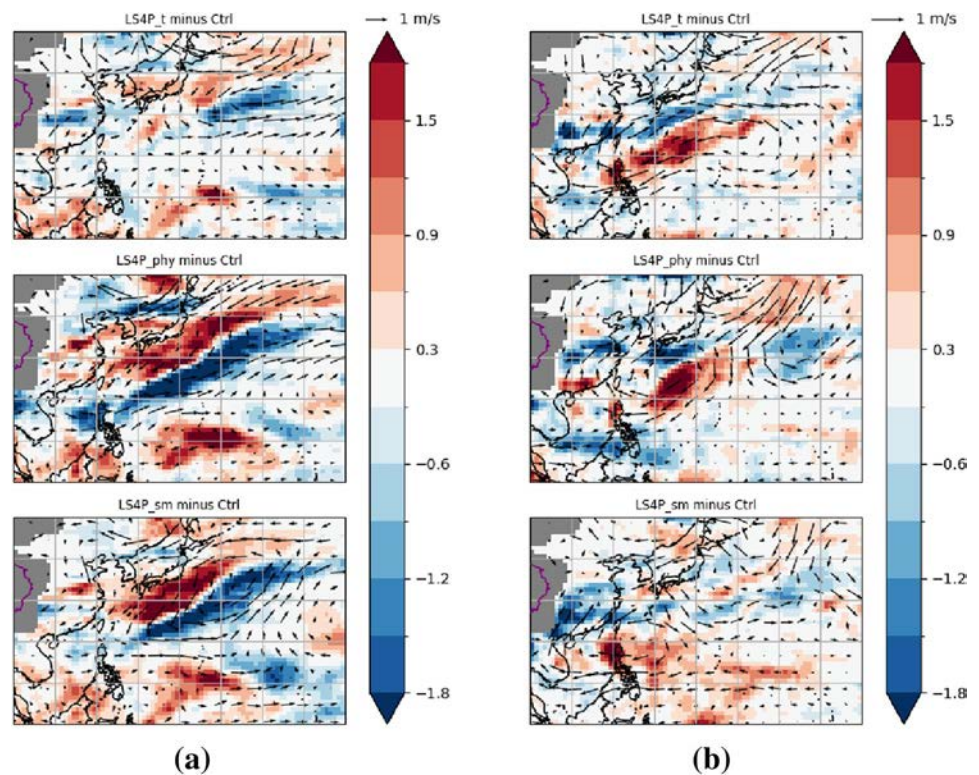
forecasts. The rationale of LS4P is to mitigate the initial sub-surface temperature bias affecting this high altitude region in order to make the most out of this source of extended range atmospheric predictability. In this pilot study focusing on a 2-month forecast initialized on May 1st 2003, we compared three initial adjustment strategies over the TP to assess the impact of the physical equilibrium of land initial conditions.

Adjusting the land initialization over the TP with more thermodynamically-balanced state variables leads to marked changes in the subsequent atmospheric response. In particular, the strategy that adjusts the soil liquid water and ice content while applying the prescribed temperature correction triggers the most effective and long-lasting atmospheric response at the hemispheric scale among the three setups. This setup also better preserves the soil physical consistency and/or enthalpy at initialization. The atmospheric response translates into a an extratropical tropospheric wave train emerging from the TP propagating eastwards towards north America during the first month, and more weakly to Europe and Asia during the second month. In this study, our balanced initialization strategy improves the atmospheric circulation pattern over North America in May and Europe and East-Asia in June, with respect to an observational reference. It also interacts with the East-Asian monsoon flow by changing the location and intensity of the Meiyu-Baiu front but without any noticeable improvement.

Conversely, we find that neither the correction of initial land temperature alone nor that of initial soil moisture alone has a major impact on the atmospheric response within our model. Only the joint correction of soil moisture and temperature with physical coherence succeeds in improving the forecast in this case study. A coordinated multi-model exercise such as GLACE-2 or LS4P, but focused on this issue of land physical consistency at initialization, would be required to verify if our findings can be generalized to other models. Similarly, this paper only reports on a single case study, and thus a way forward could be to extend this exercise over multiple consecutive years, with an ad hoc temperature correction mask for the TP each year. Such a multi-year reforecast is needed to evaluate the screen-level temperature and circulation prediction skill in different regions of the Northern hemisphere. Yet, our work clearly suggests the importance of preserving the land physical equilibrium in coupled land-atmosphere numerical experiments. This question is especially acute in subseasonal and seasonal dynamical forecast systems where the land component is initialized in a fashion to approach observed states. This implies a direct or indirect data assimilation system fed by superficial observations. Therefore, a joint assimilation of both observed soil temperature and moisture while imposing a thermally-consistent state upon initialization of the land surface could lead to improved coupled sub-seasonal to seasonal forecasts.

Finally, our numerical simulations have been carried out with an interactive ocean model in order to mimick the setup of the majority of S2S forecast systems (Vitart et al. 2017). However, it is an exception among other contributing models

in the LS4P exercise. A similar set of experiments with prescribed sea-surface temperature would be worth implementing to verify the robustness of our conclusions and to better compare our results with those of other modeling systems. The limited success of the June 2003 forecast over North America in the sensitivity experiments (Sec. 3.2) could originate from a poor simulation of the seesaw atmospheric linkage between the Tibetan plateau and the Rocky Mountains, as identified by Xue et al. (2018). In the second phase of the LS4P project, we plan to apply our new initialization method over both mountain ranges simultaneously, to try and improve the model atmospheric response.

Considering the increasing refinement of the physical processes simulated in land surface models, our study makes the case for particular care to be taken in the initialization of the land component in weather-to-seasonal forecast systems, preserving the land physical consistency to the best possible extent. Additionally, this works sheds light on the soil enthalpy which may well be a serious candidate to help reconcile the tug of war between supporters of land subsurface temperature versus root zone soil moisture as the dominant driver stemming from land in subseasonal forecasts.

Declarations

References

Ardilouze C, Batté L, Bunzel F, Decremer D, Déqué M, Doblas-Reyes F, Douville H, Fereday D, Guemas V, MacLachlan C, Müller W, Prodhomme C (2017) Multi-model assessment of the impact of soil moisture initialization on mid-latitude summer predictability. Clim Dyn 49(11–12):3959–3974

Batté L, Déqué M (2016) Randomly correcting model errors in the ARPEGE-Climate v6. 1 component of CNRM-CM: applications for seasonal forecasts. Geosci Model Dev 9(6)

Beck HE, Wood EF, Pan M, Fisher CK, Miralles DG, Van Dijk AI, McVicar TR, Adler RF (2019) MSWEP V2 global 3-hourly 0.1 precipitation: methodology and quantitative assessment. Bull Am Meteorol Soc 100(3):473–500

Black E, Blackburn M, Harrison G, Hoskins B, Methven J et al. (2004) Factors contributing to the summer 2003 european heatwave. Weather 59(8):217–223

Boisserie M, Decharme B, Descamps L, Arbogast P (2016) Land surface initialization strategy for a global reforecast dataset. Q J R Meteorol Soc 142(695):880–888

Clapp RB, Hornberger GM (1978) Empirical equations for some soil hydraulic properties. Water Resources Res 14:601–604. https://doi.org/10.1029/WR014i004p00601

Decharme B, Brun E, Boone A, Delire C, Le Moigne P, Morin S (2016) Impacts of snow and organic soils parameterization on northern Eurasian soil temperature profiles simulated by the ISBA land surface model. The Cryosphere 10(2):853–877

Decharme B, Delire C, Minvielle M, Colin J, Vergnes JP, Alias A, Saint-Martin D, Séférian R, Sénési S, Voldoire A (2019) Recent changes in the ISBA-CTRIP land surface system for use in the CNRM-CM6 climate model and in global off-line hydrological applications. J Adv Modeling Earth Syst

Dee DP, Uppala SM, Simmons AJ, Berrisford P, Poli P, Kobayashi S, Andrae U, Balmaseda MA, Balsamo G, Bauer P, Bechtold P, Beljaars ACM, van de Berg L, Bidlot J, Bormann N, Delsol C, Dragani R, Fuentes M, Geer AJ, Haimberger L, Healy SB, Hersbach H, Hólm EV, Isaksen L, Kållberg P, Köhler M, Matricardi M, McNally AP, Monge-Sanz BM, Morcrette JJ, Park BK, Peubey C, de Rosnay P, Tavolato C, Thépaut JN, Vitart F, (2011) The ERA-Interim reanalysis: configuration and performance of the data assimilation system. Q J R Meteorol Soc 137(656):553–597

Dirmeyer P, Peters-Lidard C, Balsamo G (2015) Land-atmosphere interactions and the water cycle. Seamless prediction of the Earth system: from minutes to months, edited by: Brunet, G, Jones, S, and Ruti, PM 1156

Domeisen DIV, White CJ, Afargan-Gerstman H, Muñoz Ángel G, Janiga MA, Vitart F, Wulff CO, Antoine S, Ardilouze C, Batté L, Bloomfield HC, Brayshaw DJ, Camargo SJ, Charlton-Pérez A, Collins D, Cowan T, del Mar Chaves M, Ferranti L, Gómez R, González PLM, Romero CG, Infanti JM, Karozis S, Kim H, Kolstad EW, LaJoie E, Lledó L, Magnusson L, Malguzzi P, Manrique-Suñén A, Mastrangelo D, Materia S, Medina H, Palma L, Pineda LE, Sfetsos A, Son SW, Soret A, Strazzo S, Tian D, (2022) Advances in the subseasonal prediction of extreme events: Relevant case studies across the globe. Bull Am Meteorol Soc 103(6):E1473–E1501. https://doi.org/10.1175/BAMS-D-20-0221.1

Douville H (2010) Relative contribution of soil moisture and snow mass to seasonal climate predictability: a pilot study. Clim Dyn 34(6):797–818

Ferry N, Parent L, Garric G, Barnier B, Jourdain NC et al. (2010) Mercator global Eddy permitting ocean reanalysis GLORYS1V1: Description and results. Mercator-Ocean Q Newsletter 36:15–27

Fuchs M, Campbell GS, Papendick RI (1978) An analysis of sensible and latent heat flow in a partially frozen unsaturated soil. Soil Sci Soc Am J 42:379–385. https://doi.org/10.2136/sssaj1978.03615995004200030001x

Harris I, Osborn TJ, Jones P, Lister D (2020) Version 4 of the CRU TS monthly high-resolution gridded multivariate climate dataset. Sci Data 7(1):109

Hersbach H, Bell B, Berrisford P, Hirahara S, Horányi A, Muñoz-Sabater J, Nicolas J, Peubey C, Radu R, Schepers D, Simmons A, Soci C, Abdalla S, Abellan X, Balsamo G, Bechtold P, Biavati G, Bidlot J, Bonavita M, De Chiara G, Dahlgren P, Dee D, Diamantakis M, Dragani R, Flemming J, Forbes R, Fuentes M, Geer A, Haimberger L, Healy S, Hogan RJ, Hólm E, Janisková M, Keeley S, Laloyaux P, Lopez P, Lupu C, Radnoti G, de Rosnay P, Rozum I, Vamborg F, Villaume S, Thépaut JN (2020) The ERA5 global reanalysis. Q J R Meteorol Soc 146(730):1999–2049. https://doi.org/10.1002/qj.3803

Koster R, Mahanama S, Yamada T, Balsamo G, Berg A, Boisserie M, Dirmeyer P, Doblas-Reyes F, Drewitt G, Gordon C et al. (2011) The second phase of the global land-atmosphere coupling

experiment: soil moisture contributions to subseasonal forecast skill. J Hydrometeorol 12(5):805–822

Koster RD, Dirmeyer PA, Guo Z, Bonan G, Chan E, Cox P, Gordon C, Kanae S, Kowalczyk E, Lawrence D et al. (2004) Regions of strong coupling between soil moisture and precipitation. Science 305(5687):1138–1140

Koster RD, Mahanama S, Yamada T, Balsamo G, Berg A, Boisserie M, Dirmeyer P, Doblas-Reyes F, Drewitt G, Gordon C, et al. (2010) Contribution of land surface initialization to subseasonal forecast skill: First results from a multi-model experiment. Geophys Res Lett 37(2)

Liu Y, Hoskins B, Blackburn M (2007) Impact of Tibetan orography and heating on the summer flow over Asia 2 85:1–19

Masson V, Le Moigne P, Martin E, Faroux S, Alias A, Alkama R, Belamari S, Barbu A, Boone A, Bouyssel F, Brousseau P, Brun E, Calvet JC, Carrer D, Decharme B, Delire C, Donier S, Essaouini K, Gibelin AL, Giordani H, Habets F, Jidane M, Kerdraon G, Kourzeneva E, Lafaysse M, Lafont S, Lebeaupin Brossier C, Lemonsu A, Mahfouf JF, Marguinaud P, Mokhtari M, Morin S, Pigeon G, Salgado R, Seity Y, Taillefer F, Tanguy G, Tulet P, Vincendon B, Vionnet V, Voldoire A (2013) The SURFEXv7.2 land and ocean surface platform for coupled or offline simulation of earth surface variables and fluxes. Geosci Model Dev 6(4):929–960, 10.5194/gmd-6-929-2013

Orsolini Y, Senan R, Balsamo G, Doblas-Reyes F, Vitart F, Weisheimer A, Carrasco A, Benestad R (2013) Impact of snow initialization on sub-seasonal forecasts. Clim Dyn 41:1969–1982

Sampe T, Xie SP (2010) Large-scale dynamics of the meiyu-baiu rainband: environmental forcing by the westerly jet. J Clim 23(1):113–134

...Vitart F, Ardilouze C, Bonet A, Brookshaw A, Chen M, Codorean C, Déqué M, Ferranti L, Fucile E, Fuentes M, Hendon H, Hodgson J, Kang HS, Kumar A, Lin H, Liu Q, Liu X, Malguzzi P, Mallas I, Manoussakis M, Mastrangelo D, MacLachlan C, McLean P, Minami A, Mladek R, Nakazawa T, Najm S, Nie Y, Rixen M, Robertson AW, Ruti P, Sun C, Takaya Y, Tolstykh M, Venuti F, Waliser D, Woolnough S, Wu T, Won DJ, Xiao H, Zaripov R, Zhang L (2017) The subseasonal to seasonal (S2S) prediction project database. Bull Am Meteorol Soc 98(1):163–173

Voldoire A, Decharme B, Pianezze J, Lebeaupin Brossier C, Sevault F, Seyfried L, Garnier V, Bielli S, Valcke S, Alias A, et al. (2017) SURFEX v8. 0 interface with OASIS3-MCT to couple atmosphere with hydrology, ocean, waves and sea-ice models, from coastal to global scales. Geosci Model Dev 10(11):4207–4227

Voldoire A, Saint-Martin D, Sénési S, Decharme B, Alias A, Chevallier M, Colin J, Guérémy JF, Michou M, Moine MP, Nabat P, Roehrig R, Salas y Mélia D, Séférian R, Valcke S, Beau I, Belamari S, Berthet S, Cassou C, Cattiaux J, Deshayes J, H Douville H, Franchisteguy L, Ethé C, Geoffroy O, Lévy C, Madec G, Meurdesoif Y, Msadek R, Ribes A, Sanchez E, Terray L, Waldman R, (2019) Evaluation of CMIP6 DECK experiments with CNRM-CM6-1. J Adv Modeling Earth Syst 11(7):2177–2213. https://doi.org/10.1029/2019MS001683

Volonté A, Turner AG, Schiemann R, Vidale PL, Klingaman NP (2022) Characterising the interaction of tropical and extratropical air masses controlling East Asian summer monsoon progression using a novel frontal detection approach. Weather Clim Dyn 3(2):575–599

Wilks DS (2011) Statistical methods in the atmospheric sciences, vol 100. Academic press

Xu L, Dirmeyer P (2013) Snow–atmosphere coupling strength. Part II: Albedo effect versus hydrological effect. J Hydrometeorol 14(2):404–418

Xue Y, Oaida CM, Diallo I, Neelin JD, Li S, De Sales F, Gu Y, Robinson DA, Vasic R, Yi L (2016) Spring land temperature anomalies in northwestern us and the summer drought over southern plains and adjacent areas. Environ Res Lett 11(4):044018

Xue Y, Diallo I, Li W, David Neelin J, Chu PC, Vasic R, Guo W, Li Q, Robinson DA, Zhu Y et al. (2018) Spring land surface and subsurface temperature anomalies and subsequent downstream late spring-summer droughts/floods in north america and east asia. J Geophys Res 123(10):5001–5019

Xue Y, Yao T, Boone AA, Diallo I, Liu Y, Zeng X, Lau WK, Sugimoto S, Tang Q, Pan X et al. (2021) Impact of initialized land surface temperature and snowpack on subseasonal to seasonal prediction project, phase I (LS4P-I): organization and experimental design. Geosci Model Dev 14(7):4465–4494

Xue Y, Diallo I, Boone AA, Yao T, Zhang Y, Zeng X, Neelin JD, Lau WK, Pan Y, Liu Y et al. (2022) Spring Land Temperature in Tibetan Plateau and Global-Scale Summer Precipitation: Initialization and Improved Prediction. Bull Am Meteorol Soc 103(12):E2756–E2767

Xue Y, et al. (2023) The remote effect of Tibetan Plateau spring land temperature on global subseasonal to seasonal precipitation prediction and the comparison with sea surface temperature effect - The GEWEX/LS4P Phase I experiment. Clim Dyn

Zhang C, Xie S, Klein SA, Hy Ma, Tang S, Van Weverberg K, Morcrette CJ, Petch J (2018) CAUSES: Diagnosis of the summertime warm bias in CMIP5 climate models at the ARM Southern Great Plains site. J Geophys Res 123(6):2968–2992

Zhao C, Chen H, Sun S (2018) Evaluating the capabilities of soil enthalpy, soil moisture and soil temperature in predicting seasonal precipitation. Adv Atmosp Sci 35:445–456

Zhou Y, Gao S, Shen SS (2004) A diagnostic study of formation and structures of the Meiyu front system over East Asia. J Meteorol Soc Jpn Ser II 82(6):1565–1576